

# A self-powered soft triboelectric-electrohydrodynamic pump

Received: 2 May 2024

Accepted: 24 January 2025

Published online: 03 February 2025

Fangming Li<sup>1</sup>, Shuowen Sun<sup>1</sup>, Xingfu Wan<sup>1</sup>, Minzheng Sun<sup>1</sup>,  
Steven L. Zhang<sup>2,3</sup>✉ & Minyi Xu<sup>1,4</sup>✉

Soft pumps have the potential to transform industries including soft robotics, wearable devices, microfluidics and biomedical devices, but their efficiency and power supply limitations hinder prolonged operation. Here, we report a self-powered triboelectric-electrohydrodynamic pump, which combines a soft electrohydrodynamic pump driven by an electrostatic generator, specifically a triboelectric nanogenerator. The triboelectric nanogenerator collects ambient energy and converts it into high-voltage power source, allowing it to self-power an electrohydrodynamic pump and thus eliminating the need for external power supply. Using power management circuit, geometric shape optimization, and stacking methods, we achieve a maximum pressure of 4.49 kPa and a maximum flow rate of 502 mL/min. We demonstrate the pump's versatility in applications such as self-powered soft actuators, oil pumping in microfluidics, and oil purification. The triboelectric-electrohydrodynamic pump holds promising applications, and offers new insights for the development of fully self-powered systems.

Soft pumps have been extensively researched for widespread applications ranging from soft robotics<sup>1–3</sup>, microfluidics<sup>4,5</sup>, wearable devices<sup>6,7</sup>, heat transfer<sup>8</sup>, and biomedical devices<sup>9</sup>. Compared with rigid pumps, soft pumps have the advantages of being lightweight, noiseless, portable, and wearable<sup>1</sup>. A variety of principles are developed for soft pumps, such as ion-drag electrohydrodynamic (EHD)<sup>10–12</sup>, dielectric elastomer actuators (DEA)<sup>13,14</sup>, electrostatic zipping<sup>15,16</sup>, heat activation<sup>17</sup> and piezoelectric<sup>5</sup>. Among them, the electrostatic soft pump based on ion-drag EHD has advantages of low power consumption and high pumping pressure. For example, Herbert Shea et al. developed a stretchable pump with low power consumption of 100 mW<sup>18</sup>, and further developed a fiber pump, which achieved an input power density of 15 watts per kilogram<sup>7</sup>. Jun Zou et al. enabled the soft pump to be self-healing<sup>19</sup> and achieved large-area self-healing and fast response by utilizing a different electrofluid<sup>20</sup>. Despite such great progress, applications of EHD feature high voltage and high impedance; however, the power supplies used are bulky in nature, and are largely inefficient, as they need

to amplify low voltage signals into high voltage in order to power these EHD pumps. For example, the soft robot in the Mariana Trench<sup>21</sup>, which utilizes a DEA actuator that requires high voltage, operates only 45 min with a 2500 mAh battery. The fiber pump<sup>7</sup> with an excellent power consumption (0.9 W) operates 120 min with a 550 mAh battery. With this rate, the power supply needs to be constantly replaced, which limits its practical use application. Thus, the development of soft electrostatic pumps capable of autonomous operation without reliance on an external power source is essential<sup>22</sup>.

As an emerging and promising technology for energy harvesting<sup>23</sup>, the triboelectric nanogenerator (TENG), which converts mechanical energy to electricity, has been developed by Z. L. Wang in 2012<sup>24</sup>. By harvesting low-frequency environment energy sources such as wind<sup>25,26</sup>, wave<sup>27</sup>, ocean current<sup>28</sup>, and vibration energy<sup>29</sup>, TENG enables the creation of self-powered systems that can operate independently without relying on external power supplies. In contrast to the relatively low output voltage of electromagnetic generators, the TENG can produce

<sup>1</sup>State Key Laboratory of Maritime Technology and Safety, Marine Engineering College, Dalian Maritime University, Dalian 116026, China. <sup>2</sup>School of Materials Science and Engineering, Georgia Institute of Technology, Atlanta, GA 30332-0245, USA. <sup>3</sup>Robotic Materials Department, Max Planck Institute for Intelligent Systems, Stuttgart 70569, Germany. <sup>4</sup>Guangzhou Institute of Blue Energy, Knowledge City, Huangpu District, Guangzhou 510555, China.

✉ e-mail: [szhang@is.mpg.de](mailto:szhang@is.mpg.de); [xuminyi@dlmu.edu.cn](mailto:xuminyi@dlmu.edu.cn)

high voltage based on triboelectric and electrostatic induction effects, making it suitable for driving high voltage and high impedance applications<sup>30–32</sup>. Currently, high voltage applications using TENG have been realized, including oil-water separation<sup>33</sup>, air purification<sup>34</sup>, molecular mass spectrometry<sup>35</sup>, and an electronic nose system based on triboelectric discharge<sup>36</sup>. Moreover, TENG has driven DEA devices, such as a braille display<sup>37</sup>, a soft pump used in a wearable insulin pump<sup>38</sup>, as well as a soft-actuated micro-aerial-robot<sup>39</sup>. DEA is a high-impedance application that requires high voltage, demonstrating the advantage of TENG in high-voltage applications. The above combinations prove that TENG has the potential to drive electrostatic soft pumps, and serves as a self-sustaining power supply of electrostatic soft pump systems.

Herein, we report a prototype of a self-powered and 3D-printable triboelectric-electrohydrodynamic (TEHD) pump. The system integrates the TENG as a high-voltage source to power the ion-drag EHD pump for the pumping of a working fluid. In the experiment, a free-standing rotary (FR)-TENG is used, which offers the advantages of environmental energy harvesting and continuous high-voltage generation<sup>40</sup>. Through our efforts in this study, we successfully achieved an open circuit voltage of 12 kV from the TENG, which could power this EHD-pump or other high impedance devices<sup>41–44</sup>. Directly powered by the FR-TENG, the TEHD pump operates efficiently, achieves a pressure of 0.57 kPa and a flow rate of 115 mL/min.

Subsequently, the performance is enhanced with a power management circuit (PMC), resulting in a 416% increase in pressure to 2.94 kPa, and a 137% increase in flow rate to 273 mL/min. Additionally, we studied the performance improvements achieved through geometric optimization and the stackable design separately. The optimized geometry of the TEHD pump enables it to reach 4.42 kPa. The stackable design allows parallel connection of multiple TENGs and series or parallel connection of multiple EHD pumps. This configuration enhances the pump's pressure and flow rate, with parallel TENG connections increasing charge transfer and multiple EHD pumps enabling higher pressure or flow rates. To showcase potential applications, the TEHD pump is used in soft robotics, microfluidics, and oil treatment, confirming the multifunctional nature of the pump. We believe that the presented work contributes to expanding the applications of TENG in high-voltage applications and also inspires research about prolonged operation of electrostatic systems.

## Results

### Design of the TEHD pump

A conceptual diagram of the application of the TEHD pump is shown in Fig. 1a. The system is designed with an integration of FR-TENG and EHD pump, enabling the TEHD pump to have promising applications, as shown in Fig. 1a. In the field of soft robotics, the TEHD pump can be

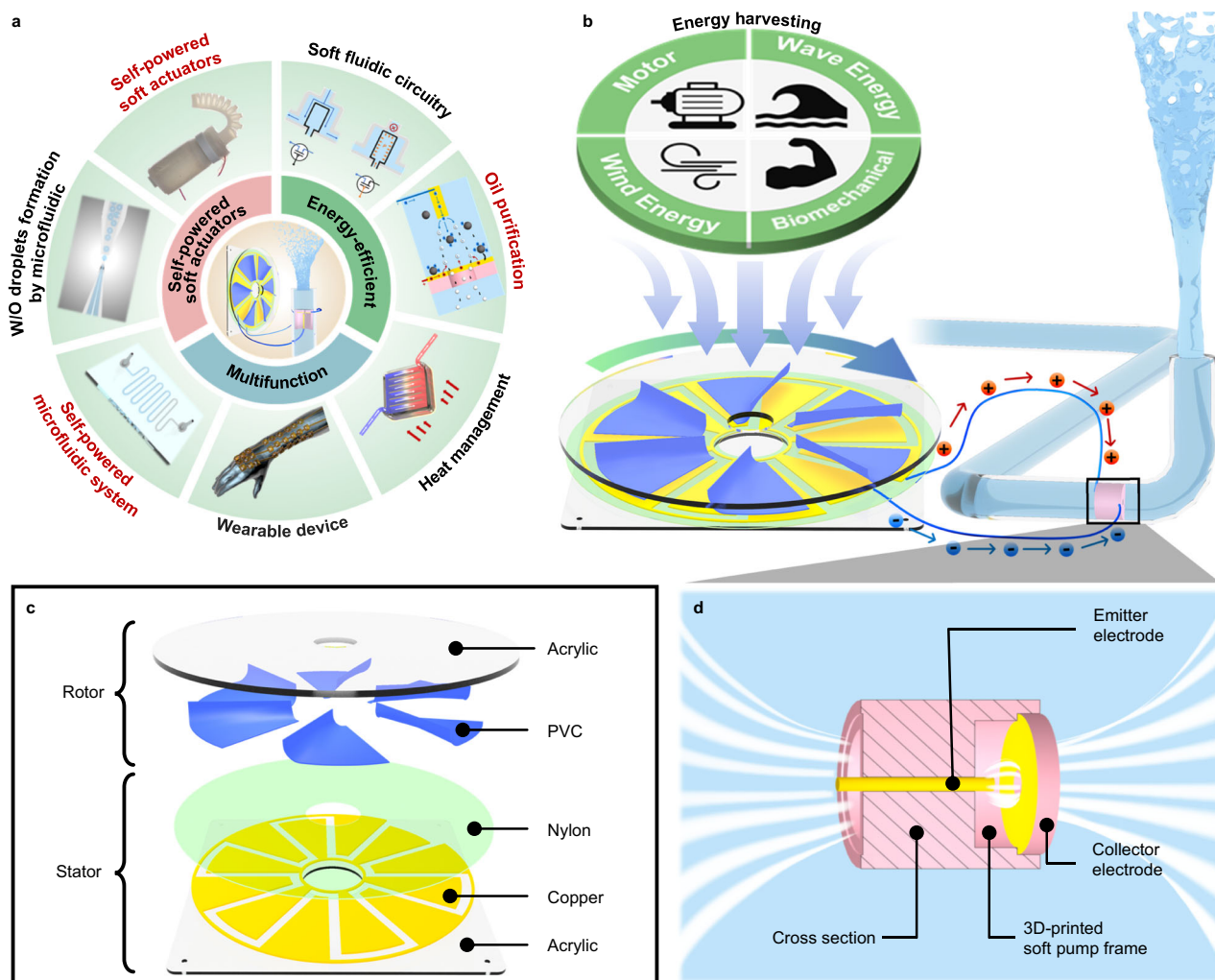


**Fig. 1 | Design of the triboelectric-electrohydrodynamic (TEHD) pump.** **a** Key features and potential applications of the TEHD pump (Applications labeled in red are demonstrated in this article). **b** Energy conversion of using the triboelectric nanogenerator (TENG), which could be driven by various mechanical energy

sources to drive an electrohydrodynamic (EHD) pump, showcasing a self-powered TEHD pump. Schematic showing the structure and materials of **(c)** the freestanding rotary TENG, and **(d)** the EHD pump.

applied to power soft actuators without external energy source and able to drive soft fluidic circuitry, such as self-opening and closing valves, in soft robots. For microfluidics, the pump can drive oil into a microfluidic chip and facilitate water/oil droplet formation, which contributes to the construction of microfluidic mobile platforms, and could be used for self-powered drug delivery systems. This TEHD pump can be utilized for oil purification and heat management, which is urgently needed for energy conservation and extending the system's lifetime and efficiency. Additionally, there is potential for applications in wearable devices, such as a self-powered driven exosuit. The applications that are highlighted in red font in Fig. 1a are all demonstrated in this paper, including self-powered soft actuator, self-powered microfluidic system, and oil purification. The self-powered property of the TEHD pump is achieved by harvesting environmental energy. As shown in Fig. 1b and Supplementary Table 1, TENG can be stimulated by any form of energy, including wind energy, ocean wave-based energy, biomechanical energy, energy from moving parts in machinery and so on. The mechanical energy harvested by TENG is converted into high-voltage electricity, thereby enabling the transfer of charges from the electrodes of the FR-TENG to the electrodes of the EHD pump. The EHD pump, enclosed in a tube containing the working fluid, injects charges into the fluid to form ions and pumps the fluid using the ion drag force exerted by the electric field. This process demonstrates how this system functions as a self-powered system, utilizing energy source directly from the environment without relying on external power supplies. Previous works have shown that TENG systems could effectively harvest environmental energy and enable self-powered applications, we present Supplementary Table 1 along with the accompanying analysis, highlighting their potential in driving the TEHD pumping system. With the self-powered capability, the TEHD pumping system could particularly impact applications such as long-duration autonomous soft robots or self-sustaining buoys in remote areas, as well as wearable devices that harness human body energy and other applications.

Figure 1c shows the structure of the FR-TENG and the materials used to fabricate the FR-TENG. FR-TENG is composed of two main parts, namely, the stator and the rotor. The stator is composed of electrodes fabricated by printed circuit board (PCB) technology, and with a surface layer of nylon film, which acts as a positive charge-trapping layer. In contrast, the rotor consists of a disk made from acrylic with floating polyvinyl chloride (PVC) film inserts, which acts as a negative charge trapping layer (detailed fabrication steps in Method section). For a more detailed understanding, Supplementary Fig. 1 provides comprehensive multi-angle images of the FR-TENG.

The EHD pump consists of the frame, emitter electrode, and collector electrode (Fig. 1d). The fabrication process of the EHD pump is demonstrated in the Method section and Supplementary Movie 1. The multiple views of the 3D-printed soft pump using TPU materials of Young's modulus of 9.4 MPa are presented in Supplementary Fig. 2. Emitter and collector electrodes are positioned on the frame, with internal channels within the frame allowing the working fluid to flow. Emitter and collector electrodes are connected to the electrodes of the FR-TENG. Under an applied electric field or voltage, charges are injected into the fluid from the emitter electrode and form charged ions with the fluid molecules. From the EHD theory<sup>45</sup>, the electric field force on the fluid by the electric field is shown by the equation:

$$\vec{F} = q\vec{E} - \frac{1}{2}E^2\nabla\epsilon + \frac{1}{2}\nabla\left[E^2\rho\left(\frac{\partial\epsilon}{\partial\rho}\right)_T\right] \quad (1)$$

where  $q$  is the charge density,  $E$  is the electric field,  $\epsilon$  is the fluid permittivity, and  $T$  is the temperature. The three terms in the equation represent the Coulomb force, the dielectric force, and the electrostriction force, respectively. In our case, since the working fluid is single phase, incompressible and under same temperature, the

Coulomb force plays a dominant role, and the equation can be rewritten as:

$$\vec{F} = q\vec{E} \quad (2)$$

According to Eq. (2), charges injected into the working fluid, along with the electric field between the two electrodes, collectively generate Coulomb forces, thereby pumping the working fluid.

### Electrical characteristics and performance of the TEHD pump

As the rotor moves to various positions, the working mechanism of the TEHD pump is divided into four stages, as illustrated in Fig. 2a; we use linalyl acetate as an example of the working fluid.

On the first stage, the PVC film is above the left electrode, and the charge on the PVC film is balanced with the charges on the nylon film and the electrode below. Also, the positive charge on the right nylon film is balanced with the right electrode underneath the film. At this moment, there is no charge transfer through the two electrodes.

On the second stage, the PVC film moves to the right as the rotor rotates, and under the effect of electrostatic induction, the electrode below the PVC film needs to have an opposite charge. This would trigger charge transfer: the positive charge moves from the left electrode to the tip of the emitter electrode and the negative charge moves from the right electrode to the surface of the collector electrode. The potential difference between the emitter electrode and collector electrode produces an electric field through the working fluid. The electric field could cause field emission<sup>46</sup>, and field ionization<sup>47</sup>, in which charges are injected into the working fluid, forming ions. Due to the action of the electric field force on ions, as explained by the Coulomb force in Eq. (2), the working fluid is dragged and pumped. When the positively charged ions near the collector electrode, negative charges on the collector electrode neutralize with positive ions in the working fluid.

On the third stage, the PVC film moves entirely above the right electrode, at which point, contrary to stage 1, electrostatic equilibrium is re-established.

On the fourth stage, the PVC film continues to move, at which point the charge flow is exactly the opposite of the second stage. Negative charges move to the emitter electrode and positive charges move to the collector electrode. Unlike stage 2, where positive charges are injected from the emission electrode into the fluid, negative charges on the emitter electrode cannot be injected into the fluid. Due to the electric field strength around the collector electrode is not strong enough, positive charges cannot be injected into the fluid either. Since there is no charge in the fluid, the working fluid can't be pumped on the fourth stage.

Figure 2b shows the multi-physics simulation results of the TEHD pump, illustrating the charge density and velocity distribution of the working fluid during the second and fourth stages. Supplementary Note 1 and Supplementary Fig. 3 show the boundary conditions set by the simulation. Supplementary Fig. 4 presents the distribution of electric potential and electric field magnitude during the second and fourth stages. The simulation results reveal that the electric field magnitude during the second and fourth stages are similar, and the distribution of electric potential is reversed. This results in a significant difference in charge density between the two stages, consequently causing the working fluid to be pumped only during the second stage. The simulation results are consistent with the mechanism described above.

The performance of the TEHD pump is studied starting from the FR-TENG. The open-circuit voltage ( $V_{OC}$ ), short-circuit current ( $I_{SC}$ ) and transferred charge ( $Q_{SC}$ ) of various FR-TENGs are measured, while the FR-TENG is not connected to the EHD pump, reflecting the intrinsic properties of the FR-TENG.

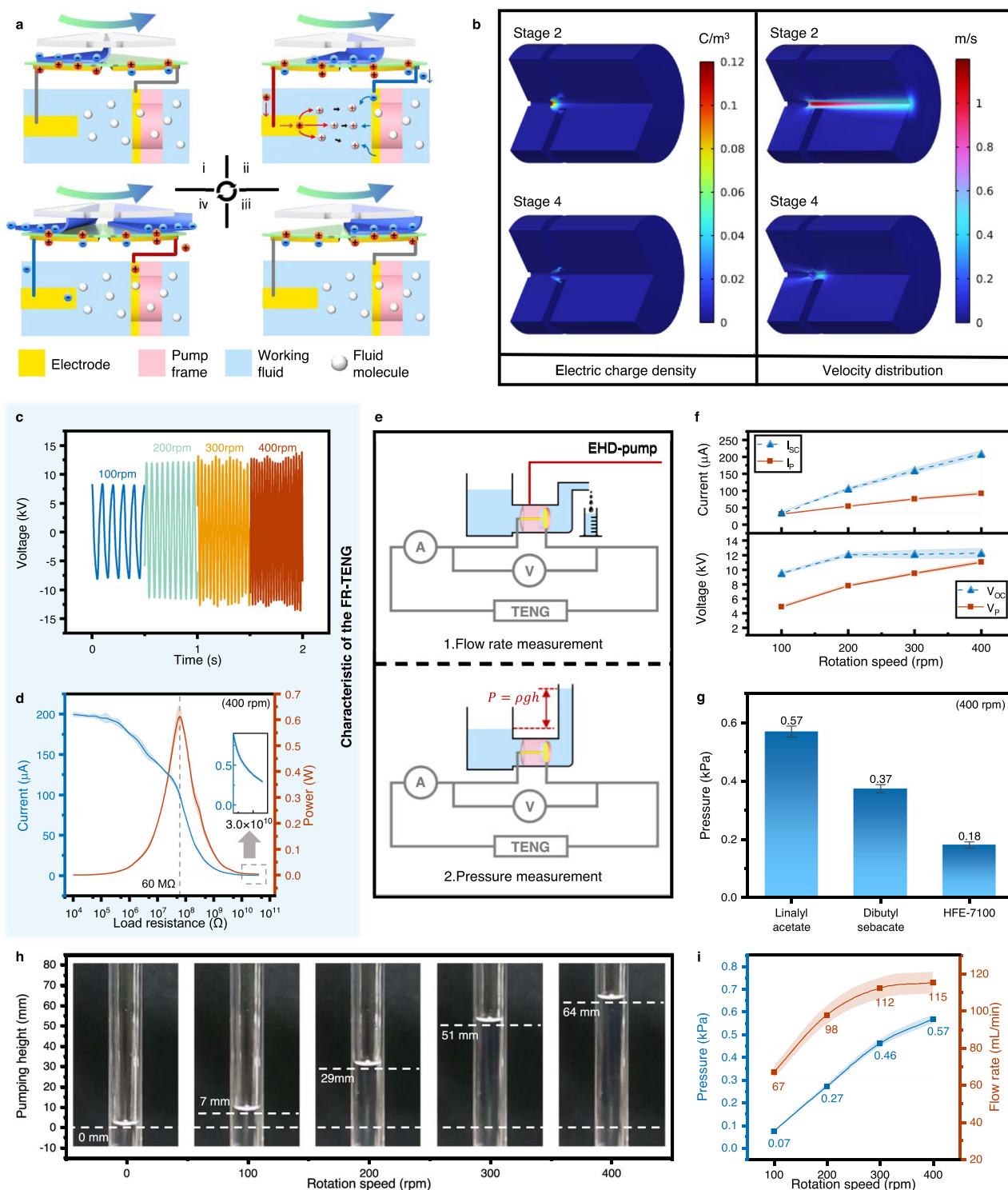


**Fig. 2 | Performance of the triboelectric-electrohydrodynamic (TEHD) pump.** **a** Working mechanism of the TEHD pump. **b** Simulation results of charge density and velocity distribution. **c** Open circuit voltage ( $V_{OC}$ ) of the freestanding rotary triboelectric nanogenerator (FR-TENG) at different rotational speeds with a 12 mm electrode gap. **d** Peak current and power at different resistances for the FR-TENG at 400 rpm. **e** Experimental platform measuring flow rate, pressure, voltage ( $V_p$ ) and

current on the pump ( $I_p$ ) during pumping. **f** Comparison of  $V_{OC}$  and  $V_p$ , and short circuit current ( $I_{SC}$ ) and  $I_p$ . **g** Pressure with different working fluids at 400 rpm. **h** Pumping height with linalyl acetate at different rotational speeds. **i** Pressure and flow rate with linalyl acetate at different rotational speeds. The data are presented as mean  $\pm$  standard deviation (SD) based on five independent experiments. Source data are provided as a Source Data file.



The selected rotation speed of the FR-TENG ranges from 100 to 400 rpm. This range is achievable through ambient energy harvesting, whether using traditional devices or TENG-based systems. Specifically, a built-in wave energy harvesting system demonstrates a power density of  $0.66 \text{ mW/cm}^3$  with a rotation speed of 1200 rpm<sup>48</sup>, while a tidal stream power system can reach a rotation speed of 950 rpm at a flow rate of  $1.2 \text{ m/s}$ <sup>49</sup>. Currently, traditional energy harvesting devices can collect abundant energy from the environment, making it straightforward to retrofit these devices with TENG technology. Moreover, in addition to the TENG strategies discussed in Supplementary Table 1, there have been significant advancements in the efficiency of TENGs for harvesting high-entropy energy<sup>50</sup>. These TENGs can effectively convert high-entropy energy by transforming irregular, low-frequency, weak mechanical energy into electricity. Additionally, the output of these devices can also be adjusted using gear mechanisms, allowing the TENG to harvest energy even in light breezes<sup>51</sup>. In summary, implementing an electrostatic pump driven by harvested ambient energy is highly feasible.

The performance of the TEHD pump is voltage-dependent, making the output voltage of the FR-TENG a crucial factor. Experiments on the electrical characteristics of FR-TENGs with different electrode gap distances (Supplementary Fig. 5) are conducted. When a sufficient amount of charges accumulates on the PVC film, the potential difference arises between the FR-TENG electrodes, leading to air breakdown between the two electrodes, as shown in Supplementary Fig. 6. This limitation restricts the maximum  $V_{OC}$  of the FR-TENG to the air breakdown voltage. Typically, breakdown voltage across air occurs at  $1 \text{ kV/mm}$ <sup>52</sup>. As shown in Fig. 2c and Supplementary Fig. 7, waveforms of  $V_{OC}$ ,  $I_{SC}$  and  $Q_{SC}$  of FR-TENGs with electrode gap distances of 8 mm, 10 mm, and 12 mm are measured, and FR-TENGs each occur air breakdown at 100 rpm, 200 rpm, and 300 rpm, limiting  $V_{OC}$  to 8 kV, 10 kV, and 12 kV. Noticeable fluctuations caused by air breakdown are observed in the waveform. A comparison of the performance of FR-TENGs is shown in Supplementary Fig. 8. Although  $V_{OC}$  increases with increasing electrode gap distance, both  $I_{SC}$  and  $Q_{SC}$  decrease. At 400 rpm, the peak value of  $I_{SC}$  of each FR-TENGs are 300  $\mu\text{A}$ , 250  $\mu\text{A}$  and 200  $\mu\text{A}$ , and  $Q_{SC}$  are 3  $\mu\text{C}$ , 2.5  $\mu\text{C}$ , and 2  $\mu\text{C}$ , respectively. The decrease of  $I_{SC}$  and  $Q_{SC}$  is caused by the decrease of electrode area due to the increased electrode gap distance. Since the TEHD pump is voltage-dependent and performance proportional to voltage, the FR-TENG with an electrode gap distance of 12 mm is chosen. The load curve of the FR-TENG at 400 rpm is shown in Fig. 2d, indicating that the equivalent internal resistance of the FR-TENG is about 60 M $\Omega$ , at which the highest output power is obtained about 0.6 W.

Subsequently, the FR-TENG is connected to the EHD pump, and the pressure, flow rate, operating voltage, and current of the TEHD pump are measured by the platform shown in Fig. 2e. In the pumping system, the FR-TENG directly drives the EHD pump, with linalyl acetate as the working fluid. As shown in Supplementary Fig. 9, waveforms of the operating voltage ( $V_p$ ) and current ( $I_p$ ) of the TEHD pump are alternating, and a comparison of them with the  $V_{OC}$  and  $I_{SC}$  is shown in Fig. 2f. At 400 rpm, the internal impedance of the TEHD pump is calculated to about 60 M $\Omega$ , similar to the equivalent internal resistance of FR-TENG—at which the output power of the FR-TENG reaches the maximum, which implies that the efficiency of the TEHD pump is at its maximum. In the study, the TEHD pump successfully directly drives three kinds of fluids, as shown in Fig. 2g, linalyl acetate works the best among them and therefore is chosen for the subsequent experiments. As shown in Fig. 2h, as the rotation speed of the FR-TENG increases, the height of the fluid gradually rises to 64 mm, which correlates with the increased  $V_p$ . The pressure of the TEHD pump is obtained by calculating the pumping height of the fluid and the result together with the flow rate is shown in Fig. 2i. As the speed increases, the performance of the TEHD pump improves, reaching a pressure of up to 0.57 kPa and flow rate of up to 115 mL/min. While the efficiency of the FR-TENG in

the TEHD pump reaches its maximum, only the second stage can effectively pump. Hence, there is still room to improve the performance of the TEHD pump; thus, the fluid does not flow or exert pressure in the reverse direction. We further improve the performance by implementing other circuit elements, such as a power management circuit (PMC).

### TEHD pump enhanced by power management circuit

To further enhance the performance of the TEHD pump, the PMC is used. In this work, four different designs of PMCs were tested, which are a full-wave voltage doubler circuit (Fig. 3a), Villard circuit, half-wave voltage doubler circuit and half-wave voltage tripler circuit, with the latter three shown in Supplementary Fig. 10. The stabilized voltages of the four PMCs at 400 rpm are shown in Supplementary Fig. 11, and a comparison of the stabilized voltages with  $V_{OC}$  is shown as well. Among the four PMCs, the full-wave voltage doubler, depicted in the photograph in Supplementary Fig. 12, is the best choice for the TEHD pump (Details in Supplementary Note 2 and Supplementary Fig. 13). The waveforms of the full-wave voltage doubler at different speeds are shown in Fig. 3b. As the speed increases, the output voltage reaches saturation more quickly and the measured output voltage is higher. However, for rotational speed that occurs above 300 rpm, and after the output voltage reaches saturation, some periodic fluctuations are observed and shown in the zoomed-in waveform in Supplementary Fig. 14; this process occurs due to air breakdown between the electrodes of the FR-TENG, as the output voltage is high.

As shown in Fig. 3c, when the speed is 400 rpm, the pumping height is drastically increased from 64 mm to 330 mm with PMC, which represents a 412% improvement. Figure 3d, e shows the comparison of pumping pressure and flow rate of TEHD pump with and without PMC enhancement at different speeds. The pumping pressure with PMC reaches 0.78 kPa at 100 rpm and increases with speed to a maximum of 2.94 kPa at a rotation speed of 400 rpm. The flow rate of the TEHD pump also increases from 82 to 273 mL/min when speed increases from 100 rpm to 400 rpm.

The  $V_p$  and  $I_p$  of the TEHD pump after PMC are measured using the circuit diagram in Supplementary Fig. 15. As shown in Fig. 3f, g, the  $V_p$  and  $I_p$  are oscillating voltage/current patterns with a positive DC offset that depends on the rotational speed. We used these plots to calculate an equivalent circuit based on our capacitor values (Fig. 3h), and found that our TENG has an internal capacitance of 66 pF, and our pump has both capacitive and resistive features, with capacitance of 31 pF and 3 G $\Omega$  (Details in Supplementary Note 3).

We tested six fluids using the PMC-enhanced TEHD pump, and the measured pressures are shown in Supplementary Fig. 16 (HFE-7100 has the maximum pressure of about 3.34 kPa, while linalyl acetate had the second largest pressure of 2.94 kPa). The key parameters of these working fluids are detailed in Supplementary Table 2, and their impact on performance is discussed in the note following the table. Due to HFE-7100 being slightly toxic and requiring a fume hood, subsequent experiments are conducted using linalyl acetate.

### Geometric influences and stackability of the TEHD pump

Understanding the effect of different geometric parameters on the TEHD pump is crucial in optimizing its performance and exploring its potential applications. In this section, we investigate the influence of the geometry of the EHD pump and the combination of multiple EHD pumps with multiple FR-TENGs; this showcases that the overall performance, such as output pressure and flow rate, could be enhanced by the stackable nature of both the TENG and the EHD pump.

Some of the studied geometry parameters of the EHD pump are shown in Fig. 4a, which includes the distance between the emitter electrode and the collector electrode ( $D_g$ ), and the diameter of the circular hole in the center of the collector electrode ( $d$ ). As shown in Fig. 4b, at 400 rpm, as  $D_g$  increases, both the flow rate and pressure

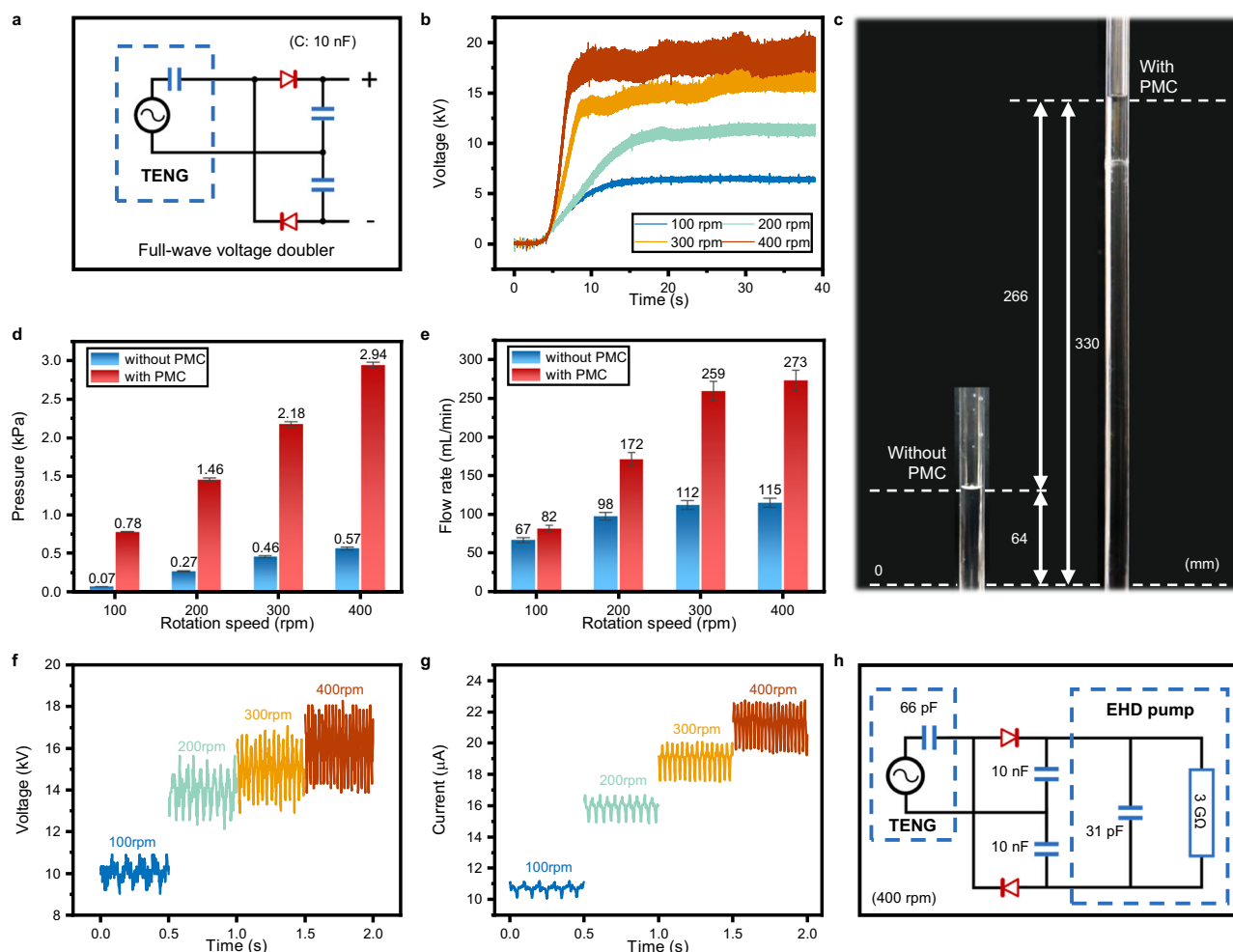


**Fig. 3 | The enhancement by power management circuit (PMC).** **a** Equivalent circuit diagram of full-wave voltage doubler. **b** Output voltage of full-wave voltage doubler at different rotational speeds. **c** Images depicting pumping height before and after the power management circuit, showing without PMC, 64 mm of linalyl acetate is pumped, and with PMC, 330 mm of working fluid is pumped. Comparison of the **(d)** pressure and **(e)** flow rate of the triboelectric-electrohydrodynamic

(TEHD) pump before and after the enhancement by the power management circuit. **f** Voltage on the pump and **(g)** current on the pump after PMC enhancement with different rotational speeds. **h** The equivalent circuit of the TEHD pump with specific value at 400 rpm. The data are presented as mean  $\pm$  standard deviation (SD) based on five independent experiments. Source data are provided as a Source Data file.

gradually decrease. Supplementary Fig. 17a, b shows the pressure and flow rate from 100 to 400 rpm with different  $D_g$  and constant  $d$  at 2 mm. When  $D_g$  is less than 1.5 mm, the breakdown between the emitter and collector electrode easily occurs, which is determined by the dielectric strength of the working fluid; this breakdown is potentially damaging to the TEHD pump, and would cause it to not work properly; thus, the lowest  $D_g$  we chose is 1.5 mm. The simulation results shown in Supplementary Fig. 17, reveal that as  $D_g$  increases, the electric field magnitude decreases,  $E = V/D_g$ , resulting in a reduced charge density, ultimately leading to a decreased performance of the TEHD pump.

Figure 4c shows the pressure and flow rate influenced by  $d$  when  $D_g$  is kept constant at 1.5 mm. The pressure and flow rate at rotational speed from 100 to 400 rpm are presented in Supplementary Fig. 18a, b. As  $d$  increases, the pressure decreases, and the flow rate increases. When  $d$  is 3.5 mm, the flow rate reaches a maximum of 387 mL/min. Simulations in Supplementary Fig. 18 illustrate that, with the decrease in  $d$ , the electric field strength, charge density, and flow velocity decrease slightly, by a much lesser extent compared to the decrease when  $D_g$  is reduced; this could be thought of as a parallel plate model and by increasing  $d$  would only increase fringe field effects, and have minimal effect on capacitance. While the total energy acquired by the fluid diminishes slightly, the Bernoulli principle

elucidates that an augmented outlet cross-sectional area results in a reduced outlet pressure and an augmented flow rate. Subsequent experiments selected  $d$  at 2 mm for higher pressure.

In addition to the geometric parameters  $D_g$  and  $d$ , we also investigated the effects of five other parameters on the TEHD pumping system: collector electrode thickness ( $T_c$ ), emitter electrode exposure length ( $L_e$ ), emitter electrode diameter ( $d_e$ ), collector electrode annular spacing ( $s$ ), and electrodes angle ( $\theta$ ). The experimental results are presented in Supplementary Fig. 19, and the photographs of all the soft pumps used to explore these geometric influences are shown in Supplementary Fig. 20. The study revealed that the emitter electrode exposure length and emitter electrode diameter had the most significant impact on enhancing pumping performance. Additionally, it is noteworthy that when  $L_e = 0$ , reverse pumping occurs, and electrode breakdown between the collector electrode and emitter electrode is observed when the reverse pumping pressure reaches 0.09 kPa. A comprehensive analysis shows that using the geometric parameters  $d = 1.5$  mm,  $d_e = 0.5$  mm, and  $L_e = 5$  mm, compared with the maximum pressure of the pump in Fig. 4b and c, resulted in an increased pumping height of 497 mm and a pressure of 4.42 kPa, as shown in Supplementary Fig. 21. The pumping process is demonstrated in Supplementary Movie 2.

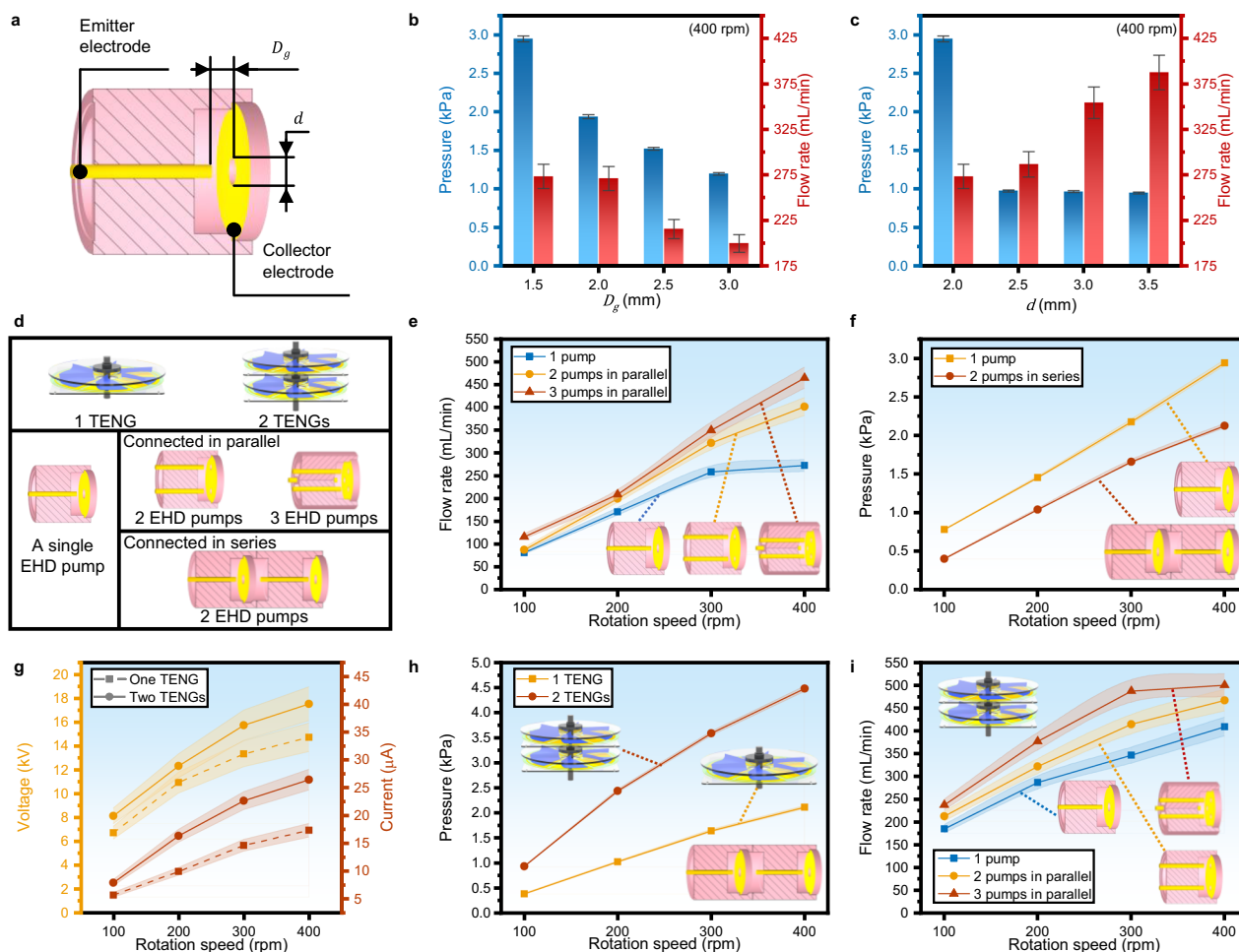


**Fig. 4 | Effect of different parameters on the triboelectric-electrohydrodynamic (TEHD) pump.** **a** Schematic showing structural parameters on the electrohydrodynamic (EHD) pump, with  $d$  the diameter of the hole on the collector electrode, and  $D_g$  the distance between the emitter electrode and the collector electrode. The trend of pressure and flow rate with **(b)** varying  $D_g$  and **(c)** varying  $d$ . **d** Schematic diagram showing the stackability of freestanding rotary triboelectric nanogenerators (FR-TENGs) and EHD pumps in the TEHD pump. FR-TENGs are connected in parallel, whereas EHD pumps are connected in both series and

parallel. **e** Flow rate and **(f)** pressure change with rotational speed when 1 FR-TENG drives multiple EHD pumps. **g** Voltage and current of the TEHD pump when driving an EHD pump with a different number of FR-TENGs. **h** Pressure comparison when driving two EHD pumps with a different number of FR-TENGs. **i** Flow rate comparison when driving different number of EHD pumps connected in parallel with 2 FR-TENGs. The data are presented as mean  $\pm$  standard deviation (SD) based on five independent experiments. Source data are provided as a Source Data file.

It is well known that pumps, when connected in parallel, have higher flow rate and when connected in series have higher output pressure<sup>53</sup>. Figure 4d shows the configuration of connecting multiple FR-TENGs in parallel and EHD pumps when connected in series or parallel. The effect on pressure and flow rate is investigated, and the results are shown in Fig. 4e, f.

When multiple pumps are connected in parallel, there is an increase in flow rate, similar to traditional pumps. At 400 rpm, the flow rate increases from 273 mL/min for a single pump to 465 mL/min for three pumps connected in parallel, but this increase is not linear with the number of pumps. However, when two pumps are connected in series, the pressure is not greater than that of a single pump. This is because when multiple pumps are connected in parallel on the circuit, the equivalent load on the PMC is decreased. From Supplementary Note 2, the voltage supplied to the pump is decreased, which results in a decreased pressure. To enhance the performance of multiple pumps, an increase in the charge supplied to the EHD pump from the FR-TENG is required. In this case, two FR-TENGs are connected in parallel to power the PMC, which runs the pump. As shown in Supplementary Fig. 22, two FR-TENGs are connected in-phase with each other and in parallel, maintaining their

$V_{OC}$ , while doubling the  $I_{SC}$ , resulting in an improvement in  $V_{out}$  of the PMC.

The TEHD pump with two EHD pumps shows a significant improvement in  $V_p$  and  $I_p$  when using two FR-TENGs, as depicted in Fig. 4g. With two pumps in series, the pressure increases from 2.13 kPa to 4.49 kPa (Fig. 4h). In the case of two pumps in parallel, the flow rate significantly increases at lower speeds and slightly increases at 400 rpm, reaching 469 mL/min (Fig. 4i). Furthermore, with three pumps in parallel, the flow rate reaches 502 mL/min. Overall, the TEHD pumping system generally enhances performance through stacking. However, as shown in Supplementary Fig. 23, performance comparisons of different stacking strategies indicate a typical decrease in efficiency. Notably, the pressure performance of 2 TENGs driving 2 pumps reaches 210.8% of a TENG driving 2 pumps in series, demonstrating increased efficiency. This occurs because the performance of the system is non-linearly related to the supplied power.

### Potential applications of the TEHD pump

With the best parameters of the pump, we show various promising applications featured in Fig. 5, such as a self-powered soft actuator, a self-powered microfluidic device, and self-powered purification of oil.



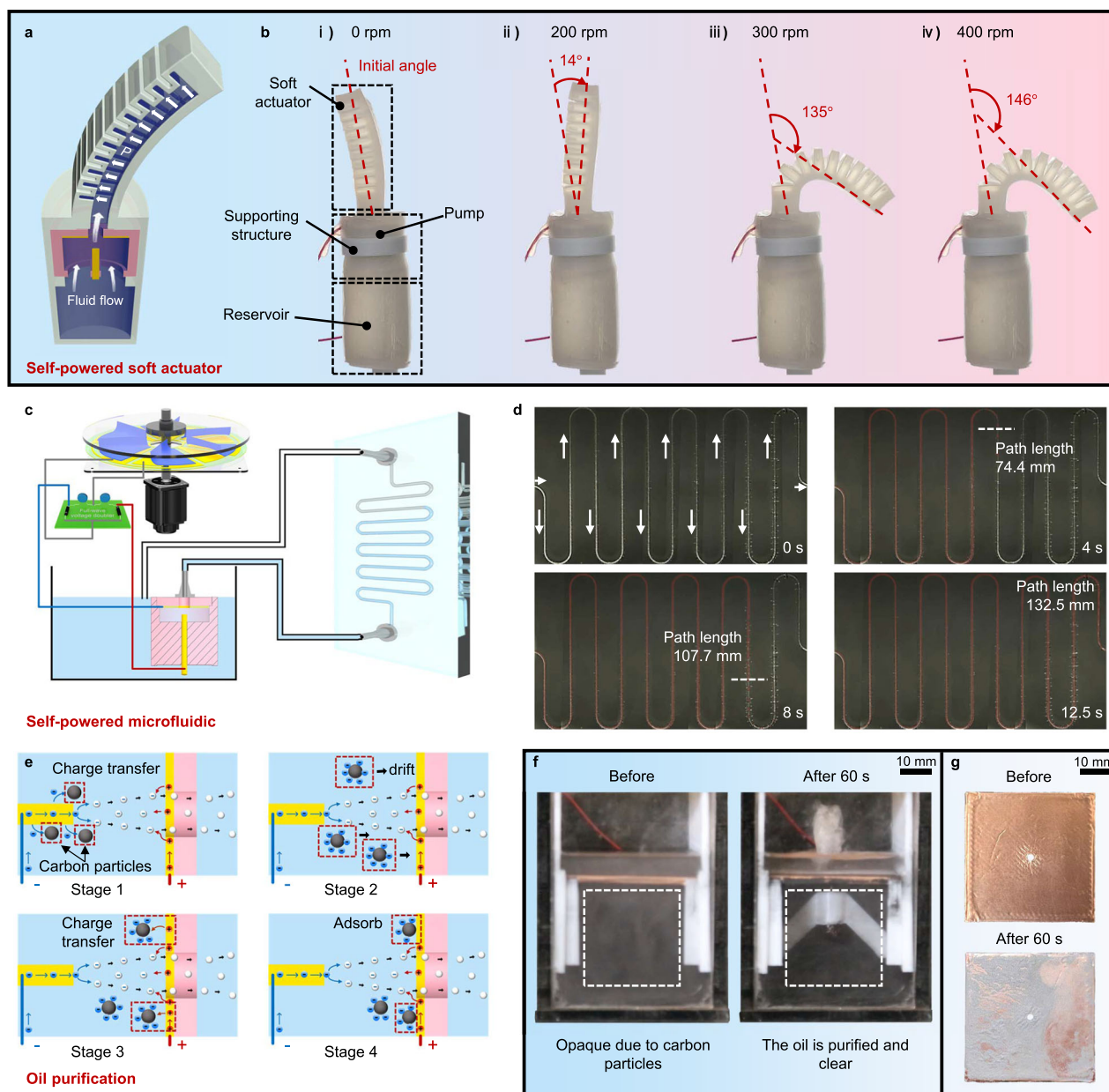


**Fig. 5 | Potential applications for triboelectric-electrohydrodynamic (TEHD) pump.** **a** Structure and principle of the soft actuator integrated TEHD pump. **b** (i) shows the structure of the soft actuator when the TEHD pump is in its initial state. (ii–iv) shows the bending angle of the soft actuator when the speed ranges from 200 rpm to 400 rpm. In (iv), with 400 rpm rotational speed, the bending angle of 146° is observed. **c** Schematic of TEHD pump driving HFE-7100

into a microfluidic chip. **d** Pumping path length over time for pumping HFE-7100 in a microfluidic chip at 400 rpm. **e** Mechanism of the TEHD pump adsorbing particles in the oil. **f** Comparison before and after 1 min of oil purification with TEHD pump driven at a rotational speed of 400 rpm. **g** Comparison of particles adsorbed on the collector electrode before and after 1 min.

For the TEHD pump driving the soft robot, we integrate a soft actuator with the soft EHD pump, as depicted in the cross-section schematic in Fig. 5a. In Fig. 5b(i), the initial structure of the soft actuator is shown. Detailed dimensions and structural information for the soft actuator can be found in Supplementary Fig. 24. As the TENG provides electricity to the pump, the TEHD pump drives the liquid from the reservoir into a channel inside the soft actuator. Under pressure from the liquid onto the channel's walls, the soft actuator begins to bend. As the rotation speed of the TENG increases to 200 rpm, the soft actuator starts bending to an angle of 14°. When the speed is raised to 300 rpm, the soft actuator undergoes more substantial bending, reaching an angle of 135°, and at 400 rpm, the angle increases to 146°. Supplementary Movie 3 demonstrates the process of

the bending of the soft actuator. The significant change in the bending angle as the speed is increased from 200 rpm to 300 rpm is a result of the combined effects, including the initiation pressure of the tentacle, the negative pressure inside the channel, and gravitational effects.

Figure 5c presents a schematic of the TEHD pump drives oil pumping in a microfluidic chip, where the channel cross-section is circular with a diameter of 0.05 mm. The actual image of the microfluidic chip is shown in Supplementary Fig. 25. The performance of the TEHD pump in pumping two fluids, linalyl acetate and HFE-7100, at various rotation speeds is demonstrated in Supplementary Movie 4. The video shows that the pumping speed of the liquids can be controlled by adjusting the rotation speed. HFE-7100, owing to its lower viscosity, exhibits higher pumping speeds compared to linalyl acetate.



Figure 5d presents the position of the fluid at different time intervals when the TENG rotates at a speed of 400 rpm. The liquid travels 132.5 mm after 12.5 seconds, showing that we can pump this liquid at a velocity of 10.6 mm/s. We anticipate that with other liquids, even faster pumping velocity could be obtained. These results demonstrate the TEHD pump has the fundamental capability to pump insulating fluids in microfluidics. By leveraging the unique capabilities of the TEHD pump, microfluidic devices can achieve enhanced portability and versatility in field-based applications.

In Fig. 5e, the TEHD pump demonstrates its potential for oil purification. When the emitter electrode of the TEHD pump injects charges into the fluid, particulate contaminants in the oil also acquire charges with the same polarity. Both the particulates and the charges in the fluid are subjected to Coulomb forces, leading them to drift to the other electrode by the applied electric field. When they reach the other electrode, particulate contaminants will be adsorbed onto the collector electrode's surface. We show this effect using an open frame and a collector electrode with a larger surface area. Supplementary Movie 5 demonstrates the effect of carbon particles being adsorbed onto the collector electrode. At this point, the oil contains 0.05 g of carbon particles. It's evident that as the TEHD pump operates, carbon particles are gradually adsorbed onto the collector electrode. Increasing the carbon particle content in the oil to 0.5 g, the contrast before and after one minute of operation is displayed in Fig. 5f. Before commencing operation, the oil is opaque as the carbon particles obstruct the frame. However, after one minute of operation, the carbon particles are adsorbed onto the collector electrode, rendering the oil transparent, and the frame becomes visible. Figure 5g illustrates the situation of carbon particle adsorption on the copper collector electrode. We could observe that the copper electrode becomes covered with gray particulates, showing the carbon is adsorbed onto the copper.

The above three demonstrations provide evidence of the potential applications of the TEHD pump, and showcase the multifunctional advantages of the TEHD pump.

## Discussion

In summary, we propose and investigate the TEHD pump, which integrates an FR-TENG as a high-voltage source to power an EHD pump, harvesting environmental energy and thereby establishing a self-powered system that operates independently of external energy sources. We showed how charges from triboelectric contact can be induced onto electrodes, causing charges to be transferred into the working fluid, facilitating pumping of the working fluid. To improve pumping performance, a power management circuit (PMC) was employed, allowing the pump to be pumped with the highest pressure achieved being 3.34 kPa for HFE-7100. We studied the impact of geometric parameters on the performance of the EHD pump, which led to an increase in the pumping pressure of linalyl acetate from 2.94 kPa to 4.42 kPa. Using the stackability strategy, we explored various combinations of modular EHD pumps and FR-TENGs. This approach successfully increased the pressure from 2.94 kPa to 4.49 kPa and the flow rate from 273 mL/min to 502 mL/min, achieved with two FR-TENGs in parallel and multiple EHD pumps connected in series or parallel. Our analysis, along with the development of an equivalent circuit model and calculation methods, provides a foundation for future research. The TEHD pump presents a self-powered, energy-efficient, and multifunctional solution for a range of applications, as demonstrated in this paper across three domains: soft robotics, microfluidics, and oil treatment. The TEHD pump has demonstrated potential, contributing to the development of next-generation sustainable soft pumps, and also provides guidelines on how to develop self-powered high voltage devices.

## Method

### Fabrication of the FR-TENG

The FR-TENG utilized in the experiments comprises of two components: the stator and rotor. The stator (thickness: 1.6 mm) is fabricated using printed circuit board (PCB) technology and it contains a grid-shaped copper electrode coating with two sets of electrodes arranged alternately, spaced 8–12 mm apart. A nylon film with a thickness of 50  $\mu\text{m}$ , serving as a tribopositive triboelectric layer, is secured to the upper surface of the electrodes with tape applied around its edges. The rotor employs a laser-cut acrylic sheet with 4 mm in thickness, forming a circular disk with an outer diameter of 320 mm and an inner diameter of 20 mm. Six evenly distributed slots, each measuring 1 mm in width and extending to a length of 107.5 mm, are radially aligned on the disk. Within each groove, a PVC film with a thickness of 100  $\mu\text{m}$  is inserted and secured with tape; the PVC serves as a tribonegative triboelectric layer. The distance between the main structure of the rotor (acrylic plate) and the surface of the stator (PCB) is set at 3 mm.

### Fabrication of the EHD pump

3D printing technology allows the formation of intricate structures in a straightforward manner, making it an extensively adopted technique for manufacturing soft devices<sup>54,55</sup>. Consequently, the frame of the EHD pump is 3D printed (Dwmaker-Z6) using TPU (PolyFlex-TPU95 by Polymaker Co.), which exhibits a tensile strength of  $29.0 \pm 2.8$  MPa, an elongation at break of  $330.1 \pm 14.9\%$ , and a Shore hardness of -95 A. The material also has a 100% modulus of  $9.4 \pm 0.3$  MPa, which provides sufficient stiffness while maintaining the necessary flexibility for the pump. However, challenges arise as the collector electrode must be constructed using conductive materials within confined spaces. Additionally, the emitter electrode takes the form of a slender cylindrical shape, and maintaining its rigidity is problematic with existing 3D printing materials, posing a challenge for single-material 3D printing techniques. We employed the “pause-embed-resume” method<sup>56</sup>, as illustrated in Supplementary Movie 1. Initially, the support structure for the collector electrode is 3D printed, onto which copper paste (JT10, Shanghai Jurong Electronics Technology Co.) is screen-printed, and then dried in ambient conditions for three hours. Copper paste was selected due to its low resistivity, in the range of 0.05–0.02 m $\Omega$ /cm<sup>2</sup>/25  $\mu\text{m}$ , ensuring efficient electrical performance. Subsequently, the overall frame is 3D printed, and when printing reaches a specific location, the copper coated collector electrode is placed into the designated position, and then the printing process continues. Finally, the emitter electrode, crafted from copper rods with varying diameters of 0.5 mm, 0.8 mm, 1 mm, and 1.5 mm, is inserted into the frame, resulting in the fabrication of a series of soft EHD pumps. Such approaches can potentially enable the development of standalone soft robotic devices which are fully compliant and with high performance. Unless otherwise specified, the default geometric parameter for the pumps is set to  $T_c = 2$  mm,  $L_e = 2$  mm,  $d_e = 1$  mm,  $s = 8$  mm,  $d = 2$  mm,  $D_g = 1.5$  mm, and  $\theta = 90^\circ$ .

### Materials for fabricating a soft actuator

The soft actuator used in the experiment is casted from silicone rubber (Dragon Skin FX-pro by Smooth-on Co.). The mold is 3D printed using PLA material. The silicone rubber's A and B components are mixed in a 1:1 volume ratio and poured into the mold, and then cured at room temperature for one hour. The silicone rubber exhibited a tensile strength of 288 psi and an elongation at break of 763%.

### Materials of different working fluids

Six different working media are used in the experiments. In the experiment, HFE-7100 is from 3 M Co. Novec™, FC-40 is from 3 M Co. Fluorinert™, linalyl acetate and dibutyl sebacate are both from Aladdin Co., 45# transformer oil is from Yamelen Co., engine oil is from Kunlun Co. Tianrun™, with the model KR6-SL10W40.

## Numerical simulations

COMSOL Multiphysics software has been used for numerical simulations, and specific details are presented in Supplementary Note 1. The physics used include: laminar flow, electric current, and charge transport.

## Measurement of electrical performance and circuit fabrication

Current measurements are conducted using a Keithley 6514 electrometer. Since the measurement voltage range of the Keithley 6514 could only go up to 200 V, the voltage is computed by measuring the current through 1 G $\Omega$  or 10 G $\Omega$  resistors (RI80 by Boniu Co., rated at 10 W and 30 kV). The Keithley 6514 can measure very small currents, with its available current ranges being 20 pA, 200 pA, 2 nA, 20 nA, 200 nA, 2  $\mu$ A, 20  $\mu$ A, 200  $\mu$ A, 2 mA, and 20 mA, allowing for precise voltage computation. For fabricating the power management circuit in Fig. 3a and Supplementary Fig. 8, the diodes used in the circuit are high-voltage diodes (HVRL400 by Gete Electronics CO.) with a repetitive peak reverse voltage of 40 kV and an average output current of 30 mA. The capacitors used in the circuit are high-voltage ceramic capacitors (30KV103 by Luyin Co.) with a voltage withstand capacity of 30 kV, and a capacitance of 10 nF.

## Data availability

The critical data supporting this study are available within the article and the Supplementary Information. Additional data related to this paper could be requested from the authors. Source data are provided with this paper.

## References

- He, Q. G. & Cai, S. Q. Soft pumps for soft robots. *Sci. Robot.* **6**, eabg6640 (2021).
- Li, M. et al. Soft actuators for real-world applications. *Nat. Rev. Mater.* **7**, 235–249 (2022).
- Wang, J. X., Gao, D. C. & Lee, P. S. Recent progress in artificial muscles for interactive soft robotics. *Adv. Mater.* **33**, 2003088 (2021).
- Mishra, N. et al. A soft wearable microfluidic patch with finger-actuated pumps and valves for on-demand, longitudinal, and multianalyte sweat sensing. *Acs Sens.* **7**, 3169–3180 (2022).
- Costa, C. M. et al. Smart and multifunctional materials based on electroactive poly(vinylidene fluoride): recent advances and opportunities in sensors, actuators, energy, environmental, and biomedical applications. *Chem. Rev.* **123**, 11392–11487 (2023).
- Gu, G. Y. R. et al. A soft neuroprosthetic hand providing simultaneous myoelectric control and tactile feedback. *Nat. Biomed. Eng.* **7**, 589–598 (2023).
- Smith, M., Cacucciolo, V. & Shea, H. Fiber pumps for wearable fluidic systems. *Science* **379**, 1327–1332 (2023).
- Greibich, F. et al. Elastocaloric heat pump with specific cooling power of 20.9 W g<sup>-1</sup> exploiting snap-through instability and strain-induced crystallization. *Nat. Energy* **6**, 260–267 (2021).
- Li, Z. W. et al. Biohybrid valveless pump-bot powered by engineered skeletal muscle. *Proc. Natl Acad. Sci. USA* **116**, 1543–1548 (2019).
- O'Connor, N., Yagoobi, J. & IEEE in Annual Meeting of the IEEE-Industry-Applications-Society (IAS) pp. 1–6 (Vancouver, CANADA; 2021).
- Tang, W. et al. Self-contained soft electrofluidic actuators. *Sci. Adv.* **7**, eabf8080 (2021).
- Zhu, P. A. et al. Liquid manipulator with printed electrode patterns for soft robotic systems. *Adv. Mater. Technol.* **8**, 2300308 (2023).
- Jiang, S. W. et al. Soft pocket pump for multi-medium transportation via an active tubular diaphragm. *Adv. Funct. Mater.* **33**, 2305289 (2023).
- Xu, S. Y. et al. A compact DEA-based soft peristaltic pump for power and control of fluidic robots. *Sci. Robot.* **8**, eadd4649 (2023).
- Leroy, E., Hinchet, R. & Shea, H. Multimode hydraulically amplified electrostatic actuators for wearable haptics. *Adv. Mater.* **32**, 2002564 (2020).
- Leroy, E. & Shea, H. Hydraulically amplified electrostatic taxels (HAXELs) for full body haptics. *Adv. Mater. Technol.* **8**, 2300242 (2023).
- Sun, J. et al. Development of a high flow rate soft pump driven by intersected twisted artificial muscles units. *Ieee Trans. Ind. Electron.* **70**, 7153–7162 (2023).
- Cacucciolo, V. et al. Stretchable pumps for soft machines. *Nature* **572**, 516–519 (2019).
- Tang, W. et al. Customizing a self-healing soft pump for robot. *Nat. Commun.* **12**, 2247 (2021).
- Tang, W. et al. Self-protection soft fluidic robots with rapid large-area self-healing capabilities. *Nat. Commun.* **14**, 6430 (2023).
- Li, G. et al. Self-powered soft robot in the Mariana Trench. *Nature* **591**, 66–71 (2021).
- Rus, D. & Tolley, M. T. Design, fabrication and control of soft robots. *Nature* **521**, 467–475 (2015).
- Zi, Y. et al. Harvesting low-frequency (<5 Hz) irregular mechanical energy: a possible killer application of triboelectric nanogenerator. *ACS Nano* **10**, 4797–4805 (2016).
- Fan, F.-R., Tian, Z.-Q. & Lin Wang, Z. Flexible triboelectric generator. *Nano Energy* **1**, 328–334 (2012).
- Wu, C. et al. Triboelectric nanogenerator: a foundation of the energy for the new era. *Adv. Energy Mater.* **9**, 1802906 (2019).
- Chen, B., Yang, Y. & Wang, Z. L. Scavenging wind energy by triboelectric nanogenerators. *Adv. Energy Mater.* **8**, 1702649 (2018).
- Zhao, T. et al. Recent progress in blue energy harvesting for powering distributed sensors in ocean. *Nano Energy* **88**, 106199 (2021).
- Deng, Z. et al. Rationally structured triboelectric nanogenerator arrays for harvesting water-current energy and self-powered sensing. *Adv. Mater.* **34**, 2205064 (2022).
- Chen, J. & Wang, Z. L. Reviving vibration energy harvesting and self-powered sensing by a triboelectric nanogenerator. *Joule* **1**, 480–521 (2017).
- Wang, J. et al. High-voltage applications of the triboelectric nanogenerator—Opportunities brought by the unique energy technology. *MRS Energy Sustainability* **6**, E17 (2020).
- Wang, X., Chen, X. & Iwamoto, M. Recent progress in the development of portable high voltage source based on triboelectric nanogenerator. *Smart Mater. Med.* **1**, 66–76 (2020).
- Nie, J., Chen, X. & Wang, Z. L. Electrically responsive materials and devices directly driven by the high voltage of triboelectric nanogenerators. *Adv. Funct. Mater.* **29**, 1806351 (2018).
- Li, F. et al. A self-powered and efficient triboelectric dehydrator for separating water-in-oil emulsions with ultrahigh moisture content. *Adv. Mater. Technol.* **7**, 2200198 (2022).
- Li, F. et al. A self-powered triboelectric negative ion generator in pipeline. *Nano Energy* **112**, 108459 (2023).
- Li, A. et al. Triboelectric nanogenerators for sensitive nano-coulomb molecular mass spectrometry. *Nat. Nanotechnol.* **12**, 481–487 (2017).
- Fu, J. et al. Deep-learning assisted biomimetic self-powered wireless electronic noses system enabled by triboelectric discharge. *Nano Energy* **121**, 109156 (2024).
- Qu, X. et al. Refreshable Braille Display System Based on Triboelectric Nanogenerator and Dielectric Elastomer. *Adv. Funct. Mater.* **31**, 2006612 (2021).
- Wei, Y. et al. Self-powered syringe pump for insulin pump therapy based on high-voltage triboelectric nanogenerator and dielectric elastomer actuator. *Adv. Funct. Mater.* **33**, 2213727 (2023).

39. Lee, Y. et al. Liftoff of a soft-actuated micro-aerial-robot powered by triboelectric nanogenerators. *Nano Energy* **126**, 109602 (2024).
40. Chen, J. H. et al. Design optimization of soft-contact freestanding rotary triboelectric nanogenerator for high-output performance. *Adv. Energy Mater.* **11**, 2102106 (2021).
41. Shen, W. et al. Sunlight-powered sustained flight of an ultralight micro aerial vehicle. *Nature* **631**, 537–543 (2024).
42. Baumgartner, R. et al. A lesson from plants: high-speed soft robotic actuators. *Adv. Sci.* **7**, 1903391 (2020).
43. Buchner, T. J. K. et al. Electrohydraulic musculoskeletal robotic leg for agile, adaptive, yet energy-efficient locomotion. *Nat. Commun.* **15**, 7634 (2024).
44. Yoder, Z. et al. Hexagonal electrohydraulic modules for rapidly reconfigurable high-speed robots. *Sci. Robot* **9**, eadl3546 (2024).
45. Woodson, H. H. & Melcher, J. R. *Electromechanical Dynamics, Part II: Fields, Forces, and Motion* (John Wiley and Sons Ltd, New York, 1968).
46. Halpern, B. & Gomer, R. Field emission in liquids. *J. Chem. Phys.* **51**, 1031–1047 (1969).
47. Halpern, B. & Gomer, R. Field ionization in liquids. *J. Chem. Phys.* **51**, 1048–1056 (1969).
48. Li, Y. et al. High-efficient built-in wave energy harvesting technology: From laboratory to open ocean test. *Appl. Ener.* **322**, 6513 (2022).
49. Usui, Y., Kanemoto, T. & Hiraki, K. Counter-rotating type tidal stream power unit boarded on pillar (performances and flow conditions of tandem propellers). *J. Therm. Sci.* **22**, 580–585 (2013).
50. Chen, B. & Wang, Z. L. Toward a new era of sustainable energy: advanced triboelectric nanogenerator for harvesting high entropy energy. *Small* **18**, e2107034 (2022).
51. Luo, Y. et al. Durability improvement of breeze-driven triboelectric-electromagnetic hybrid nanogenerator by a travel-controlled approach. *Adv. Funct. Mater.* **32**, 2205710 (2022).
52. Xiao, D. *Gas discharge and gas insulation* (Springer, Heidelberg, 2016).
53. Volk, M. *Pump characteristics and applications* (CRC Press, Boca Raton, 2013).
54. Keneth, E. S. et al. 3D printing materials for soft robotics. *Adv. Mater.* **33**, 2003387 (2021).
55. Zhang, S. et al. Fabrication and functionality integration technologies for small-scale soft robots. *Adv. Mater.* **34**, 2200671 (2022).
56. El-Atab, N. et al. Soft actuators for soft robotic applications: a review. *Adv. Intell. Syst.* **2**, 2000128 (2020).

## Acknowledgements

This work was supported by the National Key R & D Project from the Minister of Science and Technology (Grant No. 2021YFA1201604), the National Natural Science Foundation of China (Grant No. 52371345, 52101382), the “Xingliao Talent Project” of Liaoning Province

(XLYC2203175), the Dalian Outstanding Young Scientific and Technological Talents Project (Grant No.2021RJ11).

## Author contributions

S.L.Z. and M.X. supervised and guided the project; S.L.Z. and F.L. conceived the idea and designed the experiment; F.L., S.S., and X.W. fabricated the devices and performed the experiments; F.L. did the theoretical calculation; F.L., S.L.Z., and S.S. discussed the experiment and results; F.L. and M.S. wrote the manuscript; S.L.Z., F.L., and M.X. discussed and reviewed the manuscript.

## Competing interests

The authors declare no competing interests.

## Additional information

**Supplementary information** The online version contains supplementary material available at <https://doi.org/10.1038/s41467-025-56679-z>.

**Correspondence** and requests for materials should be addressed to Steven L. Zhang or Minyi Xu.

**Peer review information** *Nature Communications* thanks the anonymous reviewers for their contribution to the peer review of this work. A peer review file is available.

**Reprints and permissions information** is available at <http://www.nature.com/reprints>

**Publisher's note** Springer Nature remains neutral with regard to jurisdictional claims in published maps and institutional affiliations.

**Open Access** This article is licensed under a Creative Commons Attribution-NonCommercial-NoDerivatives 4.0 International License, which permits any non-commercial use, sharing, distribution and reproduction in any medium or format, as long as you give appropriate credit to the original author(s) and the source, provide a link to the Creative Commons licence, and indicate if you modified the licensed material. You do not have permission under this licence to share adapted material derived from this article or parts of it. The images or other third party material in this article are included in the article's Creative Commons licence, unless indicated otherwise in a credit line to the material. If material is not included in the article's Creative Commons licence and your intended use is not permitted by statutory regulation or exceeds the permitted use, you will need to obtain permission directly from the copyright holder. To view a copy of this licence, visit <http://creativecommons.org/licenses/by-nc-nd/4.0/>.

© The Author(s) 2025